1995ApJ...441..300A

THE ASTROPHYSICAL JOURNAL, 441:300–306, 1995 March 1

THE POLARIZATION AND DEPOLARIZATION OF RADIO EMISSION FROM SUPERNOVA REMNANT CASSIOPEIA A

M. C. ANDERSON, J. W. KEOHANE, AND L. RUDNICK
Astronomy Department, University of Minnesota, Minneapolis, MN 55455
Received 1993 July 29; accepted 1994 September 12

ABSTRACT

We present a study of polarimetric images of the supernova remnant Cassiopeia A at observing wavelengths of $\lambda = 6$ and 20 cm. We find that the bright ring is strongly depolarized at $\lambda = 20$ cm and conclude that this is due to a mixing of the relativistic plasma responsible for the synchrotron emission and the thermal soft X-ray–emitting material behind the reverse shock. On large scales, the magnetic field is radial in Cas A, as is common in young remnants. However, the radial field region extends well beyond the bright ring, putting constraints on the field-generating mechanism. Two interesting types of small-scale features are also found and probably reflect the same underlying phenomena; the first are features at $\lambda = 20$ cm that appear to have penetrated beyond the Faraday depolarizing shell, and the second are regions of small-scale variations in the magnetic field direction at $\lambda = 6$ cm. Both of these are likely to be identified with moderately dense clumps of stellar ejecta, leading to the bow shocks discussed by Braun, Gull, & Perley (1987) and the evolving compact features discussed by Anderson & Rudnick (1995a).

Subject headings: ISM: individual (Cassiopeia A) — magnetic fields — polarization — radio continuum: ISM — supernova remnants

1. INTRODUCTION

Given the field-freezing property of magnetized plasmas, the time history of fluid flow in a young supernova remnant (SNR) will become etched in its internal magnetic field configuration. The resulting synchrotron polarization patterns in these strong radio sources record epochs of dynamical instabilities and interactions between various ejecta components and the surrounding medium. Spatially variable depolarization may reveal regions of underlying turbulence and/or compression and heating of thermal material at various shocks within the remnant system. Studies of polarization in young remnants can thus be a fruitful means of tracing their dynamical evolution. Here, we examine the spatial patterns of polarization and depolarization in the radio emission from the young SNR Cassiopeia A and compare them to the expectations of various physical models for the thermal and relativistic plasmas.

Previous spatial comparisons of polarized and unpolarized synchrotron emission in Cas A have led to differing opinions concerning the primary depolarization mechanism in the remnant. Downs & Thompson (1972) note that the rate of depolarization between $\lambda = 6$ and 11 cm is correlated with brightness in total intensity at $\lambda = 6$ cm—they attribute this effect to enhanced internal Faraday depolarization in regions of high magnetic field strength within the source, since both rotation measure and synchrotron emissivity increase with B.

Dickel & Greisen (1979) reach a different conclusion, noting an anticorrelation between polarized and unpolarized emission at $\lambda = 11$ cm. They invoke beam depolarization as the explanation for this reverse dependence. If the magnetic field is sufficiently disordered on scales comparable to the beam size, a reduction in polarized intensity will result simply by averaging electric field vectors within the beam over many position angles. If the turbulence responsible for disordering the field is also responsible for the localized acceleration of particles (through second-order Fermi processes) and for local field amplification (through turbulent dynamo effects), the observed anticorrelation might then be expected. This argument for turbulent particle acceleration was subsequently adopted by Cowsik & Sarkar (1984), who have modeled the evolution of synchrotron emissivity in Cas A in terms of a concomitant betatron and stochastic acceleration of fresh relativistic particles during the deceleration-induced Rayleigh-Taylor instability phase. Our new analysis of Cas A depolarization models can be found in § 3.

The radial magnetic field structure in Cas A (e.g., Mayer & Hollinger 1968) and the high internal magnetic field strengths inferred from minimum energy/pressure calculations (on the order of milligauss; e.g., Rosenberg 1970) point to the existence of a large-scale field ordering and amplification mechanism at work within the remnant. Gull (1973a, b, 1975) proposed that the amplification and radial field configuration observed in most young shell remnants (see review by Milne 1987) may be a relic of an early Rayleigh-Taylor (R-T) unstable evolutionary phase accompanying the onset of ejecta deceleration. According to Gull's model, the contact surface between the decelerating ejecta and the shock-heated interstellar material behind the blast wave becomes unstable to radial perturbations when the ratio of swept-up to ejected mass exceeds 0.01. The shear flow associated with the growth of R-T fingers from this surface will preferentially align the existing field in the radial direction. Secondary Kelvin-Helmholtz instabilities generate turbulence in a thin boundary layer surrounding the fingers, creating new magnetic field energy through turbulent dynamo effects (see, e.g., Moffat 1979).

Dickel et al. (1989) have noted that, given certain physical conditions in the reverse-shocked ejecta, R-T instabilities at the contact discontinuity may be suppressed by viscosity. However, given the thermal temperatures in Cas A inferred from X-ray observations (Jansen et al. 1988) and the strong deceleration measured for the bulk radio-emitting fluid (Anderson & Rudnick 1995a, hereafter Paper II), viscosity should not greatly hinder the growth of R-T instabilities in the ejecta in this remnant. In § 4, we show and briefly discuss the extent of this radial field region.

Localized deviations from the overall radial field structure in Cas A have been attributed to perturbations caused by a clumpy component of the ejecta. Braun, Gull, & Perley (1987, hereafter BGP) point out that the field in Cas A deviates significantly from a radial configuration primarily at the tips of paraboloidal radio structures, which they have identified as bow-shocks driven by moderately dense clumps of ejecta. A similarity to bow shock models constructed by Coleman & Bicknell (1985) is cited—these models show a region of tangentially compressed field at the bow-shock apex. In § 5, we identify various groups of small-scale polarization structures.

In this paper, we take a closer look at possible polarization and depolarization mechanisms presently active in Cas A and the connection with the X-ray emitting thermal gas. Several other papers discuss closely related aspects of Cas A: The X-ray/radio correlation in Cas A is explored in detail in Keohane, Rudnick, & Anderson (1995, hereafter Paper I); the deceleration powering of radio emission on small scales is discussed in Paper II; systematic deviations from the radial magnetic field will be addressed in a later paper; an alternative relativistic particle acceleration scenario to that of Cowsik & Sarkar (1984) is introduced in Anderson & Rudnick (1995b, Paper III).

2. POLARIZATION IMAGE REDUCTION

Images of polarized intensity in Cas A at observing wavelengths of $\lambda = 6$ and 20 cm at $1\farcs3$ resolution are shown in Figure 1 (Plates 1 and 2). The visibility data used to generate these images were obtained by BGP with the Very Large Array[1] (VLA) (Napier, Thompson, & Ekers 1983)—observational details are summarized by BGP and in Table 1. Owing to the spatial complexity of the remnant, data at each observing band have been obtained in all four standard VLA configurations and combined in the final image synthesis (the A-configuration data at $\lambda = 6$ cm have been excluded in the imaging to match the resolution of the $\lambda = 20$ cm data). The typical hour angle coverage for each of the VLA observing sessions was ~9 hr. To further improve the aperture, a technique known as "bandwidth synthesis" was used, whereby data are collected at several frequencies around the nominal observing frequency.

Deconvolved images of Stokes' parameters Q and U at $1\farcs3$ resolution were generated with the Astronomical Image Processing System (AIPS) maximum entropy routine UTESS (a variation of the task VTESS, but designed to handle images which legitimately contain both positive and negative values). These images were combined to form the maps of polarized intensity displayed in Figure 1. They have been corrected for primary beam attenuation and for the Ricean bias introduced by adding in quadrature two images with Gaussian error distributions (see Killeen, Bicknell, & Ekers 1986), assuming equal noise values in Q and U of 0.3 mJy beam^{-1} at $\lambda = 20$ cm and 0.2 mJy beam^{-1} at $\lambda = 6$ cm.

Given the bandwidth synthesis techniques used here, our full bandwidth measurements of polarized intensity may be sensitive to bandwidth depolarization. At $\lambda = 6$ cm, the full range in λ^2 is approximately 0.00053 m^2 (see Table 1); based on the depolarization models of Downs & Thompson (1972), we expect only a few percent reduction due to averaging across this range. At $\lambda = 20$ cm, however, the synthesized bandwidth covers a range of 0.013 m^2. Given our particular choice of observing frequencies, the expected bandwidth depolarization is given approximately by sinc (0.02RM) where RM is the rotation measure in units of rad m^{-2}. This approximation is appropriate out to the observed high-frequency RM of ≈100 rad m^{-2}, as discussed below, where the polarization will drop by a factor of 2.

TABLE 1

SUMMARY OF EPOCH 1985 VLA OBSERVATIONS

Array	Date	Frequencies (MHz)	Bandwidth (MHz)	Integration (Time (s)
		$\lambda = 6$ cm		
B	1985.29	4640, 4970	6.25	10
C	1985.72	4832, 4902	12.5	30
D	1986.04	4816, 4866	12.5	30
		$\lambda = 20$ cm		
A	1985.16	1381, 1456, 1536, 1626	3.125	10
B	1985.29	1381, 1626	6.25	10
C	1985.72	1482, 1512	12.50	30
D	1986.04	1446, 1496	12.50	30

In order to reduce the effects of bandwidth depolarization and to determine rotation measures more accurately, we have also produced maps using only a single observing frequency. Most of these maps are of lower quality than the full synthesis maps because they use only partial data from one or two of the VLA configurations; appropriate errors are quoted on any results from comparisons of these reduced coverage maps.

3. THE INFLUENCE OF THE PLASMA ON THE LARGE SCALE POLARIZATION

3.1. *Polarized Intensity Images at* $\lambda = 6$ cm

In total intensity images (see, e.g., BGP), the emission from Cas A is dominated by a bright ring, at a radius of ≈100″. Outside of this ring is a faint plateau of diffuse emission, with some small-scale components superposed. The bulk of the polarized intensity at $\lambda = 6$ cm is distributed in a broad and stringy ring (see Fig. 1*a*) which overlaps and peaks, at most position angles, slightly outside the total intensity ring. Most of the stringy features are oriented radially, as is the magnetic field. The mean degree of polarization in the diffuse plateau region is ~8%–10%, while in the ring the fractional polarization drops to ~5%. This value is comparable to that seen at $\lambda = 2$ cm (Mayer & Hollinger 1968; Rosenberg 1970), so we conclude that any wavelength-dependent depolarization is small at $\lambda = 6$ cm and that the low fractional polarization implies considerable magnetic field disorder on small scales.

The polarized emission forms a reasonably intact ring in this $\lambda = 6$ cm image, lacking the pronounced gaps evident in the $\lambda = 11$ cm polarization image of Dickel & Greisen (1979; see their Fig. 2). Indeed, as is indicated by Figure 2 here, there is no evidence for an anticorrelation between polarized and total intensity at $\lambda = 6$ cm. This is still true at 8″ resolution, the resolution of Dickel & Greisen's $\lambda = 11$ cm image.

Furthermore, there is no significant anticorrelation between the *fractional* polarization and the total intensity at $\lambda = 6$ cm. Figure 3 shows the distribution of fractional polarization with total intensity at $1\farcs3$ resolution (pixels with uncertainties in fractional polarization exceeding ~2 σ have been excluded

---

[1] The Very Large Array is a facility of the National Radio Astronomy Observatory, operated by Associated Universities, Inc., under contract with the National Science Foundation.

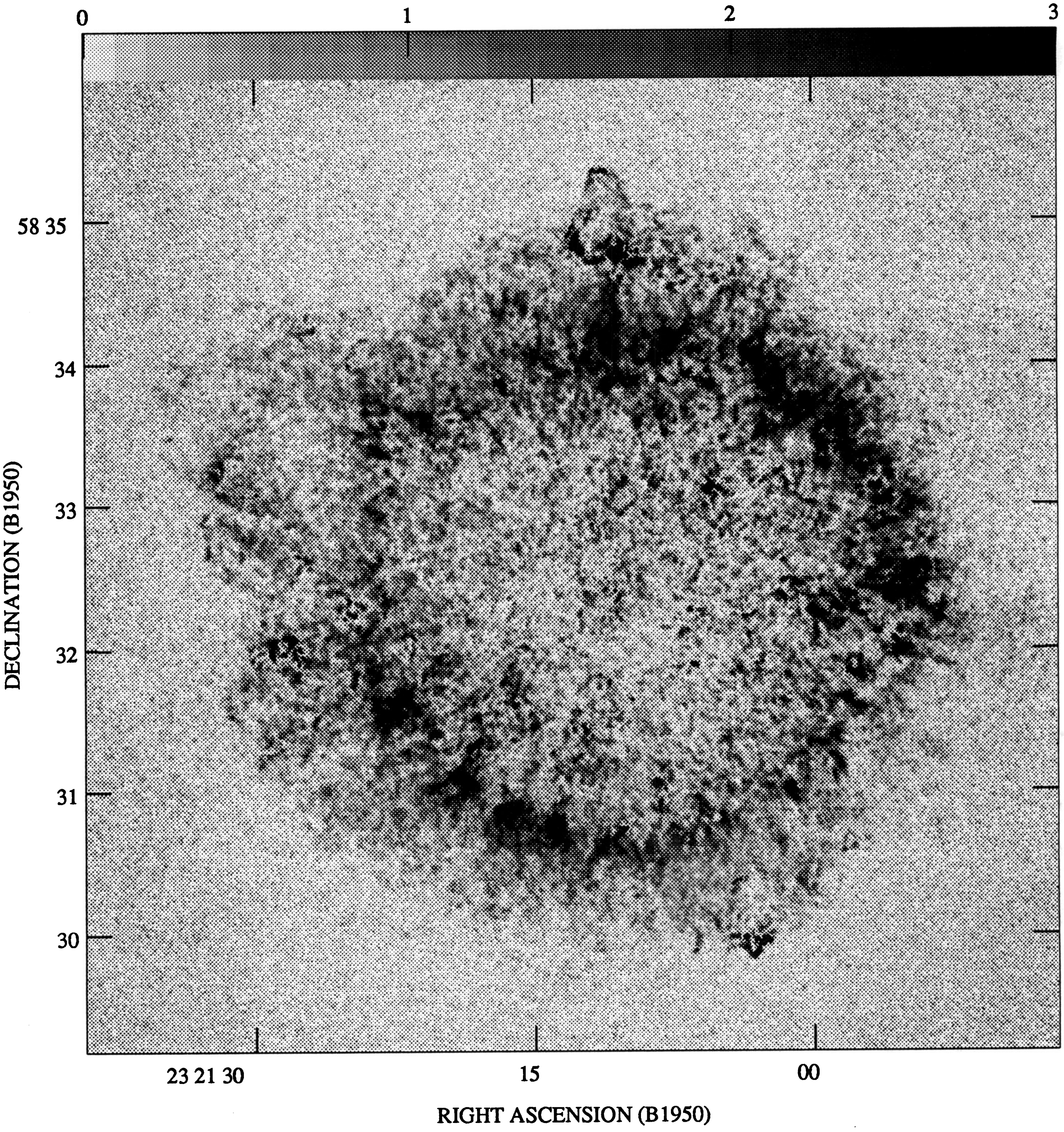

FIG. 1*a*

FIG. 1.—Distribution of 1″.3 resolution polarized intensity in Cas A (*a*) at $\lambda = 6$ cm and (*b*) at $\lambda = 20$ cm, obtained using the full synthesized bandwidth (gray-scale flux range is in units of mJy beam^{-1}).

ANDERSON, KEOHANE, & RUDNICK (see 441, 301)

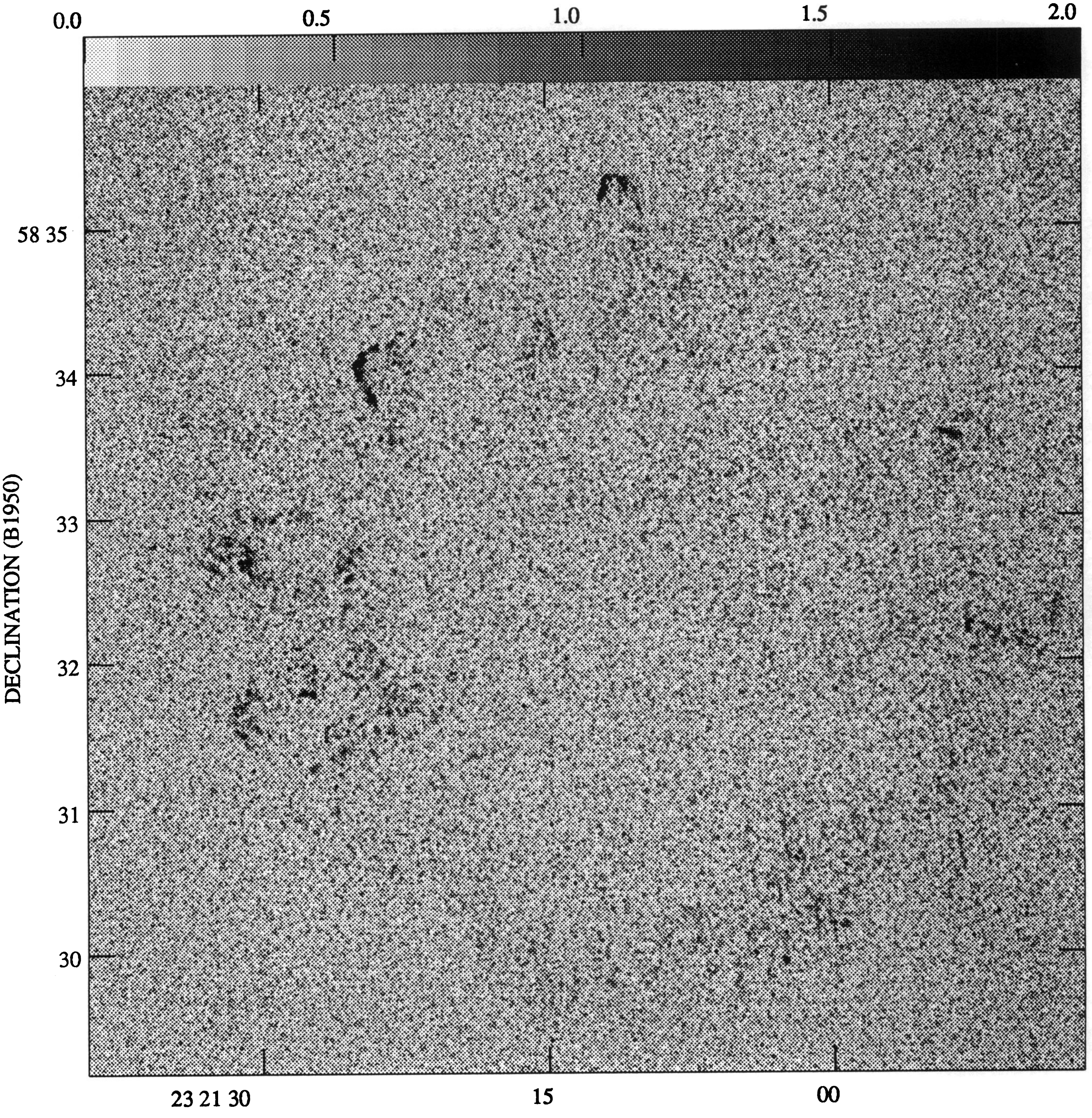

FIG. 1*b*

ANDERSON, KEOHANE, & RUDNICK (see 441, 301)

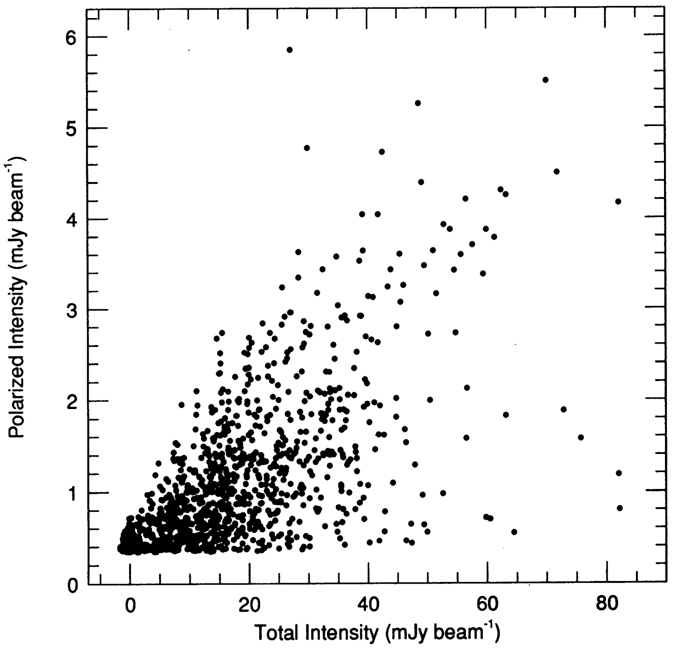

FIG. 2.—Polarized intensity vs. total intensity at $\lambda = 6$ cm, 1.'3 resolution (one point per ~7 beams is plotted).

from this plot, as they are particularly vulnerable to the Ricean bias). The crosses represent the average fractional polarization computed in bins in total intensity. Below ~40 mJy beam^{-1}, the effects of the curved lower cutoff bias the average fractional polarization, and the apparent trend is spurious. Above ~40 mJy beam^{-1}, where the effects of the lower cutoff are negligible, there is no correlation between average fractional polarization and total intensity. We thus have a situation where an anticorrelation between polarized and total intensities is found at long wavelengths (Downs & Thompson 1972; Dickel & Freisen 1979) but not at $\lambda = 6$ cm. If the long-wavelength depolarization were due to increased turbulence in the high-intensity regions, then the shorter wavelength data should show the same effect. Other explanations for the depolarization must be sought.

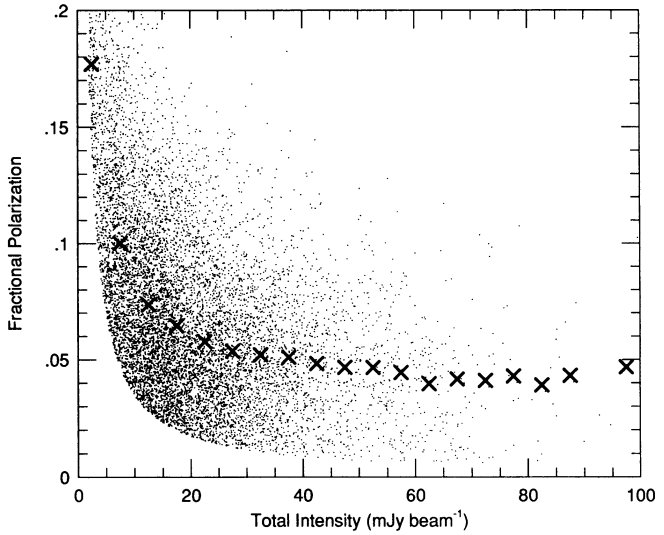

FIG. 3.—Fractional polarization vs. total intensity at $\lambda = 6$ cm (points with fractional polarization of magnitude $<2\,\sigma$ have been excluded, yielding the curved lower cutoff). One point per 2 beams is plotted. Crosses indicate the average fractional polarization computed in bins in total intensity over all independent points. The averages below ~40 mJy beam^{-1} are biased by the cutoff; above this value, the fractional polarization is seen to remain constant with total intensity.

3.2. *Depolarization at $\lambda = 20$ cm and the X-Ray Connection*

Figure 1*b* shows a map of polarized intensity at $\lambda = 20$ cm, constructed with the full synthesized bandwidth, spanning 245 MHz. Most of the synchrotron emission from Cas A has been depolarized at this wavelength, with fractional polarizations in the bright ring marginally detected at ~0.3%. The surviving polarized flux resides mostly in a number of arclike configurations (see § 5) found primarily outside the total intensity ring.

Before discussing detailed depolarization mechanisms, we note that such patterns of wavelength-dependent depolarization are most likely to be due to a thermal plasma associated in some way with the synchrotron emitting plasma. An extensive thermal plasma has been mapped in X-rays and can be compared with the depolarization data. Overlaying the $\lambda = 20$ cm polarization map and the *ROSAT*/HRI map (~keV energies, 8" resolution) shows that the polarized radio arcs fall at or beyond the lowest detectable X-ray emission (with one or two regions probably seen in projection). A more dramatic demonstration of the connection between these two plasmas is shown in Figure 4, where we compare the depolarization between $\lambda = 20$ cm and $\lambda = 6$ cm to the soft X-ray intensity as a function of radius. To produce this plot, we averaged the fractional polarization at each radio wavelength in rings at a fixed radius. We then divided these azimuthal averages to calculate a characteristic depolarization, %pol($\lambda = 20$ cm)/%pol ($\lambda = 6$ cm), at each radius. The correspondence between the depolarization and the X-ray brightness is excellent, suggesting strongly that these soft X-rays map out the thermal depolarizing medium. A similar conclusion was reached by Matsui et al. (1984) for the Kepler SNR, albeit with a small number of data points. In order to uncover the spatial/physical relationship between the relativistic and thermal plasmas, we must look at the details of the depolarization and rotation measure behavior.

3.3. *Depolarization Models and Rotation Measures*

We begin by evaluating the importance of bandwidth depolarization, where the Faraday rotation of the polarization

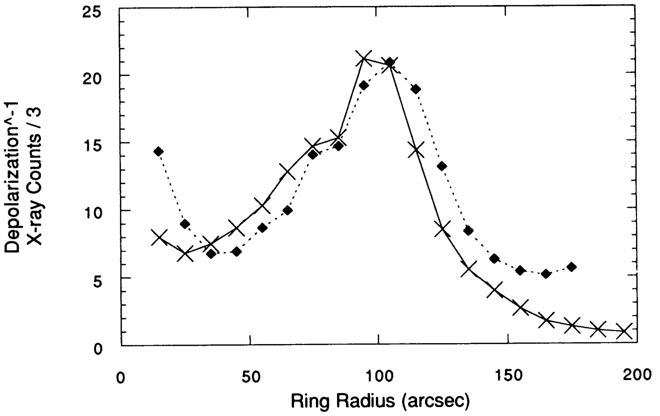

FIG. 4.—Depolarization^{-1} = %pol($\lambda = 6$ cm)/%pol($\lambda = 20$ cm) and X-ray brightness (*ROSAT*/HRI) averaged over azimuthal rings and plotted as a function of radial distance from the center of the remnant.

angle within the observing bandwidth is large enough to cause partial cancellation of the polarized flux. To explore this, we first produced a map using only the B-configuration data at 1381 MHz, which would be reasonably sensitive to both small- and large-scale features. The result was very similar to that using the full bandwidth; the bright total intensity ring remained heavily depolarized, and the same set of polarized peaks seen in Figure 1*b* appear in the narrow bandwidth map.

With a higher sensitivity to low surface brightness emission, the effects of bandwidth depolarization become visible. We compare the polarized intensities from two 15″ resolution maps in Figure 5, one generated using the full bandwidth, and the other using only data at 1482 MHz (C-configuration) and 1496 MHz (D-configuration). Over much of the bright ring, the polarized emission is reduced by about 30% by increasing the bandwidth to the full range, while some points, primarily from the northwest section, suffer up to a 50% reduction.

The above results indicate that bandwidth depolarization is important, but not the only source of depolarization at $\lambda = 20$ cm. At $\lambda = 6$ cm, 15″ resolution, the percentage polarization is ~5% around the entire bright ring. Even in the narrow bandwidth maps at $\lambda = 20$ cm, we find 0.45% polarization in the northwest and 0.3% in the southeast, consistent with the source-averaged quantities quoted by Downs & Thompson (1972).

Two additional mechanisms provide possible explanations for the factor of ~10 depolarization to $\lambda = 20$ cm correlated with the structure of the remnant. The first is variations on scales smaller than the beam size in the Faraday depth of a thermal shell surrounding the bright radio shell; the second is a Faraday thick thermal medium actually mixed with the relativistic plasma. These two may be distinguished using Faraday rotation information—a sufficiently well-resolved external screen will show a λ^2 dependence to the polarization position angle; a mixed plasma will not (e.g., Laing 1984).

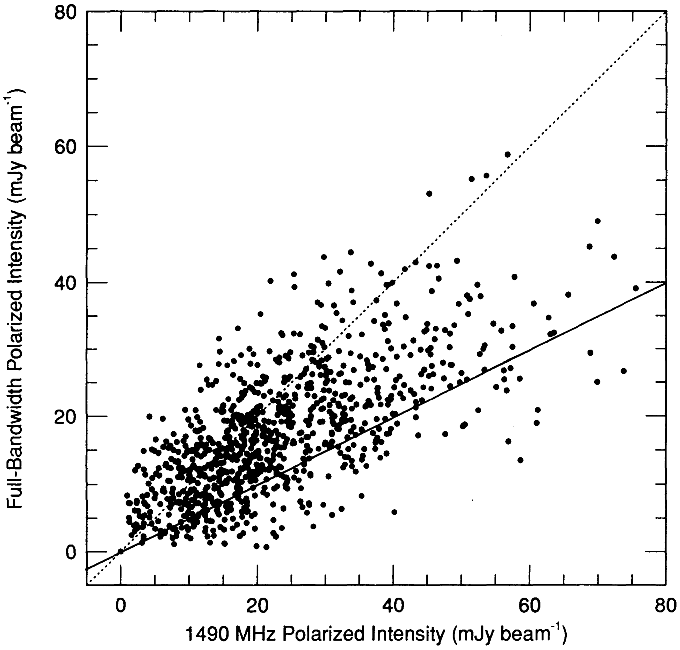

FIG. 5.—Pixel-to-pixel comparison (one point per beam) of polarized images constructed from only data at ~1490 MHz (C- and D-configuration, *horizontal axis*) and from the full synthesized bandwidth (*vertical axis*). Lines of 0% depolarization and 50% bandwidth depolarization are shown.

We first look at the rotation measure derived using $\lambda = 6$ cm information alone. The largest frequency separation existed for our A-configuration observations, so we made separate polarization maps at 4640 MHz and 4970 MHz. These were convolved at a resolution of 5″, in order to improve the signal-to-noise ratio. The map of the difference in polarization position angle, $\Delta\chi$, between the two frequencies showed an average value of $-3^\circ\!.4 \pm 0^\circ\!.75$, corresponding to a rotation measure of -110 ± 25 rad m^{-2}. This value is consistent with the value of -130 rad m^{-2} determined by Rosenberg (1970) between $\lambda = 2$ cm and $\lambda = 6$ cm. The exact value of the high frequency rotation measure is still unclear; it is hard to assess the errors in Rosenberg's determination, and the calibration of our absolute polarization angle is likely to be uncertain by at least 1° (33 rad m^{-2}).

Spatial variations in the rotation measure can be studied with much higher accuracy, since they do not depend on the absolute position angle. After examining the behavior of $\Delta\chi$ as a function of polarized flux density, we conclude that there are no statistically significant spatial variations in our $\lambda = 6$ cm data—the scatter is consistent with that arising from random noise. In order to put a quantitative limit on spatial variations, we looked at all points with a polarized flux above 20 mJy beam^{-1} and compared the northwest and southeast regions. These two quadrants are the brightest in polarized flux and showed the largest difference in their $\lambda = 20$ cm bandwidth depolarizations. We found median values of $\Delta\chi \sim -2^\circ\!.7$, $-2^\circ\!.9$, respectively, corresponding to a difference in rotation measure of less than 6 rad m^{-2}. The $\lambda = 6$ cm data therefore suggest that the Faraday depth is quite uniform across the face of the remnant.

A completely different picture emerges at $\lambda = 20$ cm. To measure rotation measures here, we made separate polarization maps at each of the four frequencies used in the A configuration (see Table 1), convolved to a resolution of 5″ to improve signal-to-noise ratios. Approximately 12 compact regions had sufficient signal-to-noise ratios so that an accurate rotation measure could be determined from a single beam; these are discussed in § 5. For the rest of the map, we performed a least-squares fit for rotation measure at each point on map, using the AIPS task RM, and blanked the resulting image of derived rotation measures wherever the error was greater than 30 rad m^{-2}. Large-scale coherent areas of quite different mean rotation measures were visible on this map. The scatter of rotation measures within these ~50″–100″ areas is consistent with noise; we found only isolated cases of significant small-scale deviations from the larger-scale mean value. We identified approximate boundaries for these coherent regions and made histograms and determined the mean rotation measure in each region. The results of this analysis are shown in Figures 6 and 7.

None of these rotation measure regions has a mean value which is consistent with that derived at $\lambda = 6$ cm. This indicates that the polarization position angle cannot follow the λ^2 behavior. It is therefore likely that the depolarization mechanism is a thermal plasma physically mixed with the relativistic plasmas, as opposed to an irregular Faraday screen.

We have already shown that the large-scale depolarization behavior follows the X-ray brightness in Figure 4. The coupling between these two plasmas is also evident in Paper I, where we demonstrate that, after correction for interstellar absorption, the *ROSAT*/HRI image of Cas A correlates strongly with radio brightness. Thus we expect that bright

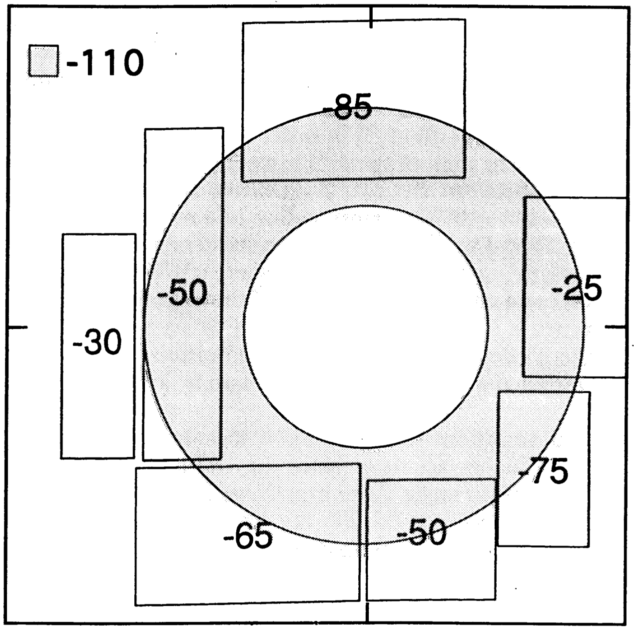

FIG. 6.—Rotation measure regions in Cas A. The shaded ring represents the average rotation measure determined at $\lambda = 6$ cm. The boxes are coherent regions of rotation measures from the four-frequency $\lambda = 20$ cm data.

regions of synchrotron radiation, which then indirectly imply high corresponding thermal densities as well as high magnetic fields, should be the most strongly depolarized. The depolarizarion at $\lambda = 20$ cm (6 cm) is so strong (weak), that we cannot perform this test using our data. However, this correlation between radio brightness and depolarization is what was identified much earlier by Downs & Thompson (1972) at $\lambda = 11$ cm, and we verify here their suggestion of internal Faraday rotation as the depolarizing mechanism. Downs & Thompson (1972) suggested an electron density of $n = 2$ cm^{-3} to explain the depolarization—this is consistent with the value $n = 1.4$ cm^{-3} obtained in applying a reverse shock model to the observed soft X-ray luminosity and temperature (McKee 1974). All of these results are consistent with the data of Dickel & Greisen (1979) discussed previously; however, we have now shown that it is not their suggested turbulence in the bright regions, but mixing of the thermal and relativistic plasmas that is responsible.

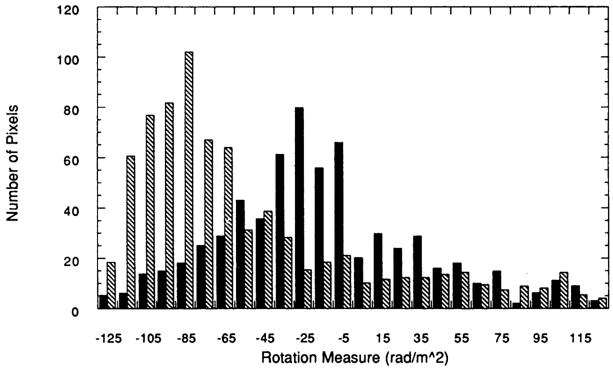

FIG. 7.—Histograms of least-squares fit rotation measures within two of the different rotation measure regions shown in Fig. 6; the shaded columns are from the region marked -30 rad m^{-2}; striped columns are from the -85 rad m^{-2} region.

We comment briefly on this radio/X-ray linkage. Such behavior is expected if the same underlying physical process underlies both emission mechanisms. For example, locally enhanced deceleration can result in increased synchrotron emissivity (Paper II) and would also be accompanied by a locally strengthened reverse shock and increased X-ray emission. An explanation for the large-scale variations in rotation measure at $\lambda = 20$ cm is not evident and may await more detailed information from a wavelength around $\lambda = 11$ cm to allow modeling of the coupled plasmas.

4. THE LARGE-SCALE MAGNETIC FIELD

The distribution of polarization position angle in Cas A has typically been displayed only for regions in the remnant with high polarized signal (e.g., BGP). In Figure 8 (Plate 3) we show the distribution over the entire remnant, retaining pixels with low signal-to-noise ratio to emphasize the large-radius corrugated boundary which separates regions of coherent polarization angle from regions of pure noise. Polarization angles in Figure 8 have each been rotated to a coordinate system where a position angle of zero represents a purely radial magnetic field (tangential electric field), measured with respect to the center of the bright radio ring. The mean deviation from the radial direction is approximately $-24°$, as expected at $\lambda = 6$ cm from the high-frequency rotation measures. In addition, there are systematic large-scale departures from the radial direction; these will be discussed in a separate paper.

The most striking aspect of Figure 8 is the lack of evidence for the bright ring (demarcated by the overlaid circle) in the distribution of position angles. The annular width of the ring is only $\sim 30''$, but it sits on a broad base of total and polarized flux $\sim 100''$ wide. Except in the north, there is no change in the radial field as one passes through the bright, narrow ring into what is normally referred to as the plateau region. In Gull's (1975) model for radial field alignment in young SNRs, the radial field region defines how far R-T fingers extend from the contact discontinuity (Gull predicts a dominant length scale comparable to the stand-off distance of the outer shock). These data can be used to test detailed hydro- and magnetohydrodynamical models which show the evolution of R-T and other instabilities in young shell remnants (Jun & Norman 1994; Cliffe & Jones 1994).

It is also interesting to note that the region of coherent field in the northeastern sector of the remnant extends without discontinuity into the "jet" region, the place where there is a gap in the bright ring and diffuse emission visible out to at least 220″ from the center. Optical (van den Berg & Kamper 1985) and radio emission knots (Paper II) in this region show significantly higher proper motions than do knots in other parts of the remnant, perhaps indicating an asymmetric ejection of material in the supernova event. In the Gull (1975) model, then, R-T fingers appear to extend freely into the hole bored by jet material into the ambient medium. However, since the total intensity radio shell appears partially broken in this direction, it is not clear where the contact surface (from which R-T fingers are thought to form) is and how it might have evolved.

5. SMALL-SCALE POLARIZATION FEATURES

In addition to the overall polarization structure, there are a number of more compact regions where the magnetic field direction varies over small scales. We have isolated such localized deviations in polarization angle in the following way.

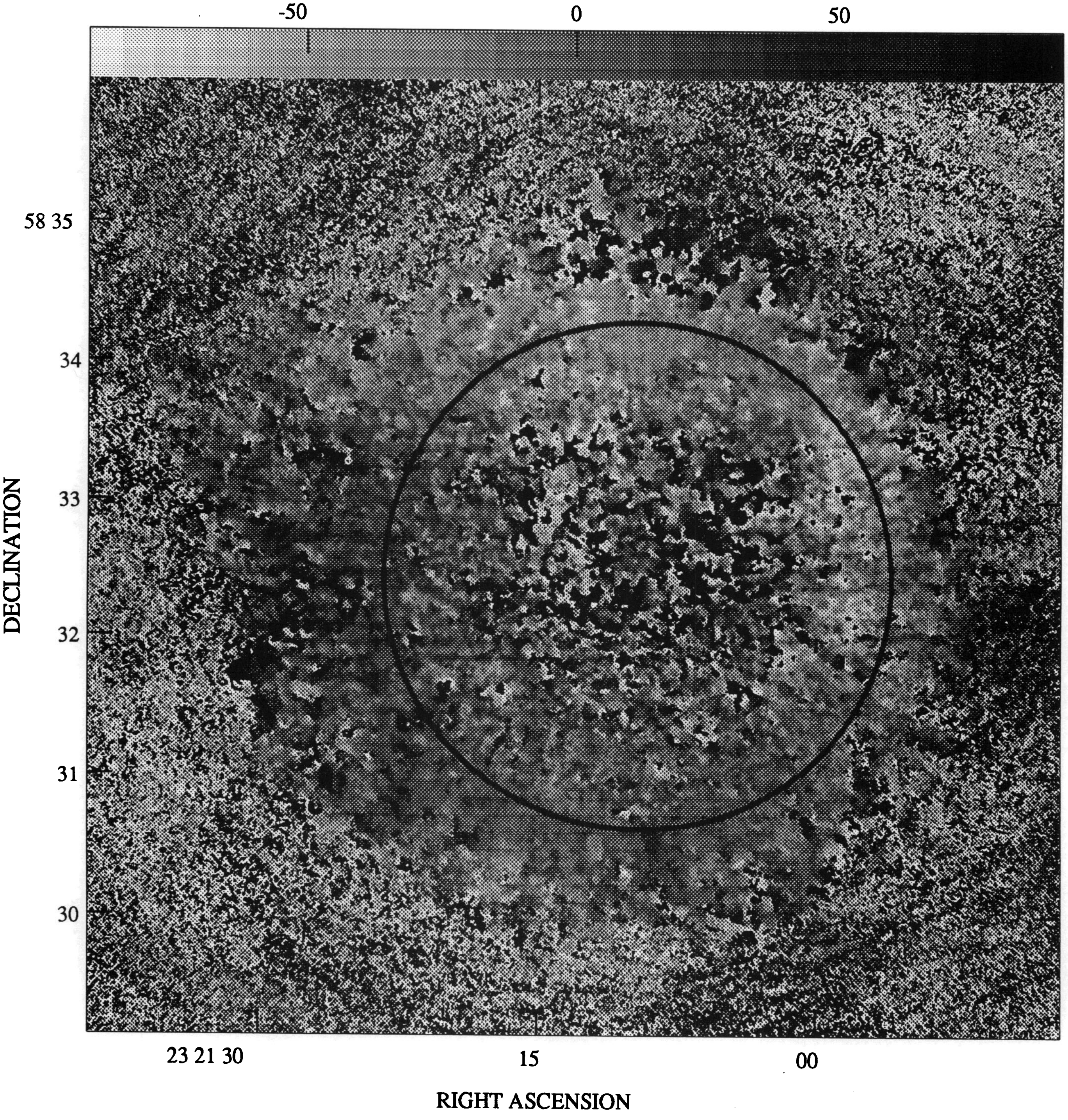

FIG. 8.—Distribution of polarization position angle in Cas A at $\lambda = 6$ cm. Polarization angles have been rotated to reflect deviations from a locally tangential orientation, measured with respect to the center of the radio shell. Zero degrees in this plot therefore represents a purely tangential electric field orientation (and therefore a radial magnetic field, in the absence of Faraday rotation effects). The overlaid circle represents the approximate size and position of the shell.

ANDERSON, KEOHANE, & RUDNICK (see 441, 304)

1995ApJ...441..300A

Maps of Stokes' parameters Q and U at 1″.3 resolution were convolved to 5″, then added in quadrature to form an image of polarized intensity. A map of polarized intensity was also generated directly from a quadrature sum of the 1″.3 resolution Q and U maps, then convolved to 5″. These two images are very similar in most parts of the remnant, except in those regions where the polarization angle is rapidly changing—there the preconvolution of Q and U has diminished the resultant polarized intensity by averaging over many angles within the 5″ convolving beam.

Figure 9 (Plate 4) shows the difference between the post- and preconvolved polarized intensity images of Cas A. Bright structures in this image indicate regions where polarized intensity has been degraded by 30%–70% in the act of preconvolution. Overlaid is a schematic rendering of the 11 "bow shocks" identified by BGP. Most of these features do indeed correspond to regions of rapid angle change. As a group, the "bow shock" features identified by BGP are particularly bright in polarized intensity, with fractional polarization ranging between 15% and 20% at $\lambda = 6$ cm. These features likely constitute faint radio emission from regions of order magnetic field at bow shocks driven by clumpy ejecta, as predicted by the synchrotron models of Coleman & Bicknell (1988) and Jones, Kang, & Tregillis (1994).

Several other compact structures in total intensity are highlighted in Figure 9. In particular, the string of radio knots which trace the southern edge of the jet (indicated by star symbols) are quite distinctive. If the jet represents a region of faster ejecta outflow, then shear forces at the boundary of the jet may trigger vortical instabilities which would both amplify the field, producing the radio knots, and perturb the local field structure.

One of the strongest features in Figure 9 corresponds to a bright knot embedded in the radio ring to the south—a similar feature is found in the ring to the northeast (both are indicated with daggers). Such structures are interpreted in Paper II as clumps of ejecta just beginning to decelerate, here because of interaction with the strongly decelerated diffuse ejecta shell. Two additional groups of features exhibiting large angle rotations are seen; one lies near the center of the shell and one at the base of the northern bow shocks—these are loosely associated with structures in total intensity.

Another, partially overlapping, set of small-scale polarization features is found in the $\lambda = 20$ cm map (Fig. 1*b*), where the bright, diffuse ring has been almost completely depolarized. A number of distinct crescent- or arc-shaped features are seen, with percentage polarizations between 7%–15%. These arcs are, in hindsight, also apparent in the $\lambda = 6$ cm polarized intensity image in Figure 1*a* but are not readily identifiable in the midst of the strong polarized ring emission. The spectral indices in these features, in polarized intensity, are consistent with the integrated total intensity spectral index of the remnant. It is likely that they would not have been identified as features of interest had it not been for the presence of a spatially selective depolarization screen. We can safely assume that many additional faint structures of this type remain undetected.

More detailed $\lambda = 6$ cm images of two of these features are shown in Figure 10 (Plate 5). Neither of these features has a well-measured rotation measure, since the polarization angle at 5″ resolution does not follow a λ^2 behavior. To correct for the average rotation measure at high frequencies of -110 rad m^{-2}, the angles in this figure should be rotated by $\sim 24°$ counterclockwise. The inferred magnetic fields are predominantly tangential to the arcs, as expected in the bow shock picture.

We can also study the rotation measures of the compact features that appear in the $\lambda = 20$ cm polarization maps. Using the individual frequency A-configuration maps discussed previously, we were able to determine rotation measures for approximately 12 distinct features. Rotation measures from -25 to $+70$ rad m^{-2} were found, extending far beyond the values that had been measured using either the $\lambda = 6$ cm data or the large-scale $\lambda = 20$ cm results. These features are also depolarized, to varying extents. The wavelength dependence of the polarization for the two features showing the extreme rotation measure values is shown in Figure 11. All of these results indicate that compact radio features that have penetrated the depolarizing shell also carry a thermal component with them. A very rough estimate of 4 cm^{-3} for the thermal density can be obtained by assuming a rotation measure of ~ 50 rad m^{-2}, a equipartition magnetic field of ~ 100 μG and a path length comparable to the feature sizes of $\sim 10^{17}$ cm.

6. CONCLUSIONS

We conclude that the pattern of depolarization observed in Cas A is most consistent with internal Faraday depolarization by soft X-ray-emitting thermal material mixed with the synchrotron emitting plasma. This is most clearly demonstrated by the strong correlation between depolarization and X-ray

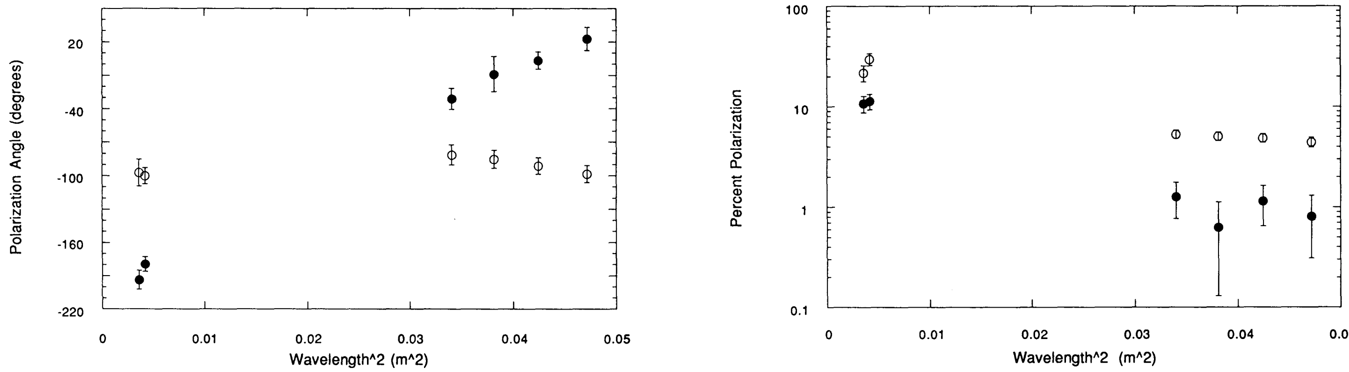

FIG. 11*a* FIG. 11*b*

FIG. 11.—Wavelength dependence of polarization for two compact features seen in $\lambda = 20$ cm polarization maps, 5″ resolution. One feature shows a λ^2 dependence all the way to $\lambda = 6$ cm; the other does not. (*a*) Polarization angle; (*b*) fractional polarization.

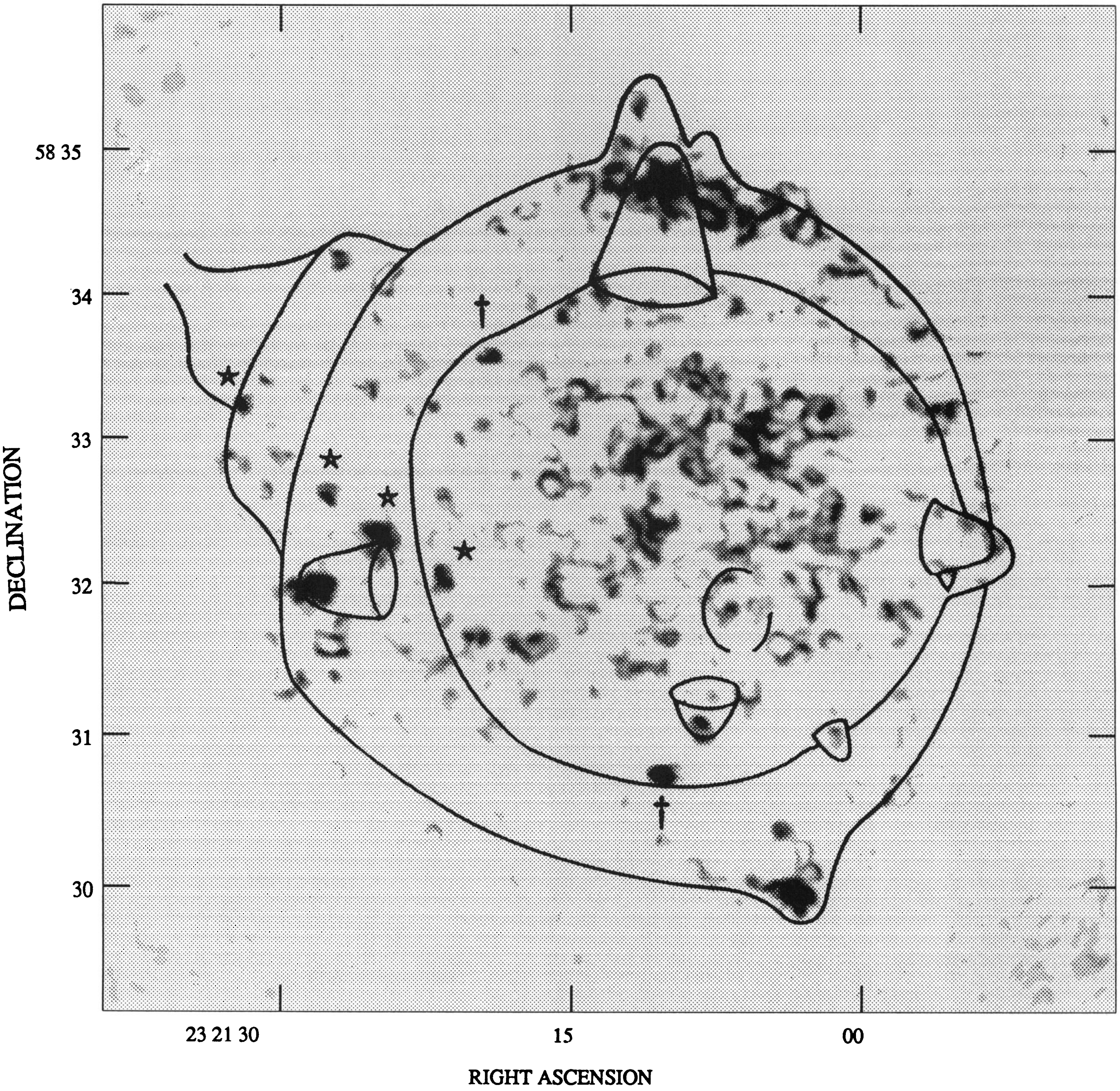

FIG. 9.—Difference between post- and preconvolved images of polarized intensity (see discussion in text). Overlaid are schematics demarcating BGP's 11 "bow shocks" (*solid lines*; from BGP) and symbols identifying new features discussed here.

ANDERSON, KEOHANE, & RUDNICK (see 441, 305)

1995ApJ...441..300A

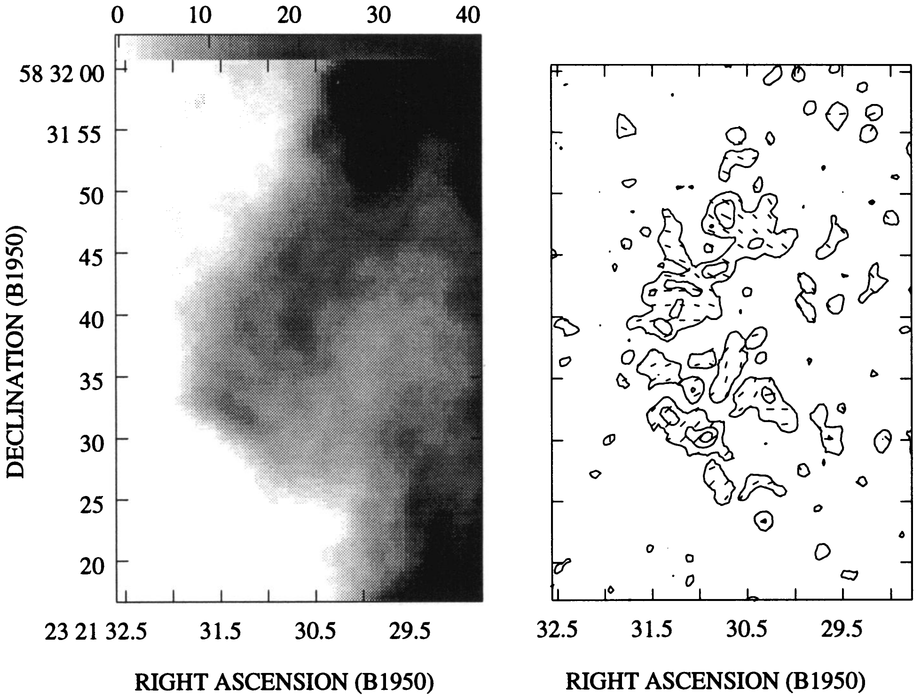

FIG. 10*a*

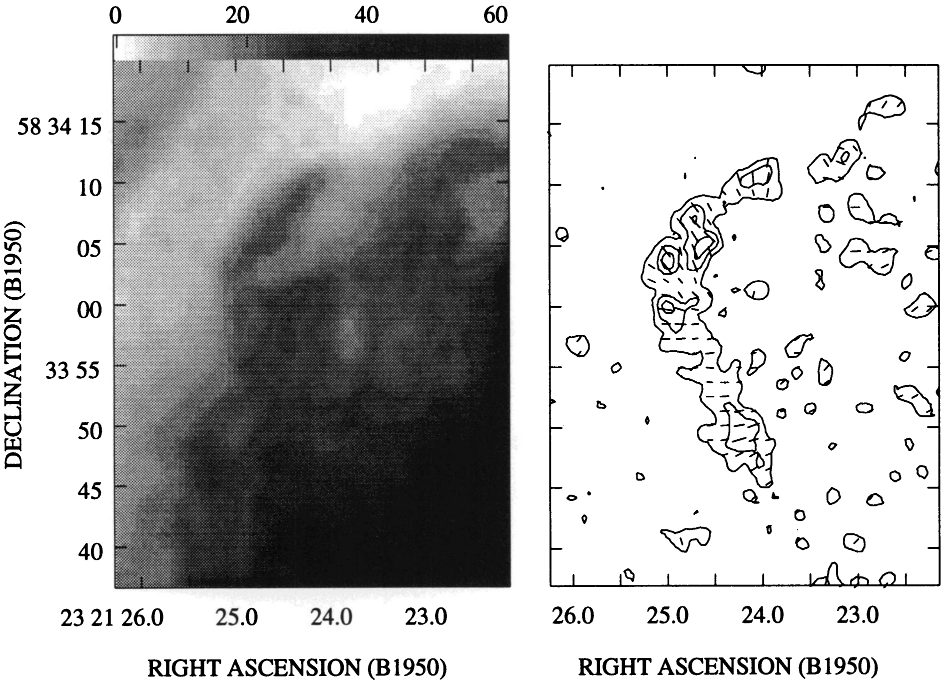

FIG. 10*b*

FIG. 10.—Total and polarized emission from two "arc" structures, prominent in polarized intensity at $\lambda = 20$ cm. These arcs are difficult to see in total intensity (*gray scales*), forming the faint leading edge of a low brightness region. Arcs are located (*a*) in the northeastern part of the remnant, and (*b*) in the east-southeast. The gray scales, contours, and vector magnitudes reflect measurements at $\lambda = 20$ cm (full synthesis bandwidth), while the polarization vector angles (uncorrected for RM) are derived from $\lambda = 6$ cm.

ANDERSON, KEOHANE, & RUDNICK (see 441, 305)

brightness and by the non-λ^2 behavior of the polarized emission. The correlation between radio and X-ray brightness (Paper I) leads to a correlation between depolarization and radio brightness as well, but the increased turbulence and particle acceleration invoked by Dickel & Greisen (1979) and Cowsik & Sarkar (1984) is not needed.

New, faint crescent-shaped features similar to previously identified bow shocks have been found in polarized intensity at $\lambda = 20$ cm. We are able to see these structures only because surrounding high surface brightness emission has been depolarized. If these structures are indeed bow shocks, driven by clumps of ejecta, then they can be very faint in total intensity, and there are certainly many such shocks that are not readily seen. Such a plethora of shocks may provide fertile grounds for the acceleration of particles within the remnant. Other compact regions of disturbed field are also seen at locations where they may be interacting with large-scale structure. The role of compact clumps in particle acceleration and magnetic field generation is developed further in Paper III.

A lower limit to the physical extent of radial field alignment in Cas A can be deduced from maps of polarization angle. It is clear that the effects of the alignment mechanism penetrate at least as far as the boundary of the diffuse radio plateau and through the jet region. This observation places constraints on the nature of suitable field-generating mechanisms and can be compared with new numerical simulations.

This work was supported, in part, by the NSF through grants AST 87-20285 and AST 91-00486. We acknowledge BGP for the acquisition of the radio data presented here. We also thank the referee, Rick Perley, for suggesting significant improvements to this work. This research has made use of data obtained from the US *ROSAT* Public Data Archive, which is jointly managed by the *ROSAT* Science Data Center and the HEASARC. The HEASARC is a collaboration of the Laboratory for High Energy Astrophysics and the NSSDC at NASA/GSFC.

REFERENCES

Anderson, M. C., & Rudnick, L. 1995a, ApJ, 441, 307 (Paper II)
———. 1995b, in preparation (Paper III)
Braun, R., Gull, S. F., & Perley, R. A. 1987, Nature, 327, 395 (BGP)
Cliffe, J. A., & Jones, T. W. 1994, BAAS, 26, 927
Coleman, C. S., & Bicknell, G. V. 1985, MNRAS, 214, 337
———. 1988, MNRAS, 230, 497
Cowsik, R., & Sarkar, S. 1984, MNRAS, 207, 745
Dickel, J. R., Eilek, J. A., Jones, E. M., & Reynolds, S. P. 1989, ApJS, 70, 497
Dickel, J. R., & Greisen, E. W. 1979, A&A, 75, 44
Downs, G. S., & Thompson, A. R. 1972, AJ, 77, 120
Gull, S. F. 1973a, MNRAS, 161, 47
———. 1973b, MNRAS, 162, 135
———. 1975, MNRAS, 171, 263
Jansen, F., Smith, A., Bleeker, J. A. M., de Korte, P. A. J., Peacock, A., & White, N. E. 1988, ApJ, 331, 949
Jones, T. W., Kang, H., & Tregillis, I. 1994, ApJ, 432, 194
June, B. I., & Norman, M. L. 1994, BAAS, 26, 925
Keohane, J. W., Rudnick, L., & Anderson, M. C. 1995, in preparation (Paper I)
Killeen, N., Bicknell, G. V., & Ekers, R. D. 1986, ApJ, 302, 306
Laing, R. A. 1984, in Physics of Energy Transport in Extragalactic Radio Sources, ed. A. H. Bridle & J. A. Eilek (Greenbank, WV: NRAO), 90
Matsui, Y., Long, L., Dickel, J., & Greisen, E. 1984, ApJ, 287, 295
Mayer, C. H., & Hollinger, J. P. 1968, ApJ, 151, 53
McKee, C. F. 1974, ApJ, 188, 335
Milne, D. K. 1987, Australian J. Phys., 40, 771
Moffat, H. K. 1979, Magnetic Field Generation in Electrically Conducting Fluids (Cambridge: Cambridge Univ. Press)
Napier, P. J., Thompson, A. R., & Ekers, R. D. 1983, Proc. IEEE, 71, 1295
Rosenberg, I. 1970, MNRAS, 151, 109
van den Bergh, S., & Kamper, K. W. 1985, ApJ, 293, 537